catalysts

MDPI

Article

A Comparative Evaluation of Physicochemical Properties and Photocatalytic Efficiencies of Cerium Oxide and Copper Oxide Nanofluids

Rashmi M. [1,2], Padmanaban R. [1], Vaithinathan Karthikeyan [3], Vellaisamy A. L. Roy [4], Anantha-Iyengar Gopalan [5], Gopalan Saianand [6], Wha-Jung Kim [5,*] and Venkatramanan Kannan [1,*]

1 Department of Physics, SCSVMV Deemed University, Kanchipuram 631561, India; mrashme@gmail.com (R.M.); kv.rjpm@gmail.com (P.R.)
2 Department of Physics, St. Joseph's College of Arts and Science for Women, Hosur 635126, India
3 Department of Materials Science & Engineering, City University of Hongkong, Hong Kong 999077, China; kvecers@gmail.com
4 Department of Electronics & Nanoscale Engineering, University of Glasgow, Glasgow G12 8QQ, UK; roy.vellaisamy@glasgow.ac.uk
5 Daeyong Regional Infrastructure Technology Development Center, Kyungpook National University, Daegu 41556, Korea; algopal99@gmail.com
6 Faculty of Engineering and Built Environment, The University of Newcastle, Callaghan NSW 2308, Australia; SaiAnand.Gopalan@newcastle.edu.au
* Correspondence: kimwj@knu.ac.kr (W.-J.K.); kv@kanchiuniv.ac.in (V.K.)

Received: 6 December 2019; Accepted: 23 December 2019; Published: 26 December 2019

Abstract: Copper oxide (CuO) and cerium oxide (CeO_2) of various concentrations have been prepared through an ultrasonically assisted dispersion of CuO and CeO_2 nanoparticles (NPs) in which water and nanofluids (NFs) were formulated. The morphological properties of the CuO and CeO_2 NPs are reported. Few of the physicochemical properties that can influence the photocatalytic activities of the NFs are evaluated, such as viscosity, activation energy, density, thermal conductivity, electrical conductivity, alternating current (AC) conductivity, pH, stability, refractive index and optical band gap of the CuO and CeO_2 NFs. Viscosity studies have been made at four different temperatures (303 K, 308 K, 313 K and 318 K) and the activation energy is calculated and compared between the CuO and CeO_2 NFs. The thermal conductivity of the two NFs is calculated and compared. Electrical conductivity is measured for CuO and CeO_2 NFs using an impedance analyzer at different frequencies at 303 K. The dielectric constant and AC conductivity were studied. The electrical conductivity and pH of the prepared NFs are measured and the results are compared. The stability of the NFs is determined from Zeta potential values obtained from dynamic light scattering measurements. UV-Visible diffuse reflectance measurements were used to deduce the optical bandgap of the respective metal oxide NPs in the NFs. The photocatalytic efficiencies of the CuO NFs and CeO_2 NFs were evaluated using methylene blue (MB) as the model dye. The rate constant for the photodegradation of MB was higher for CuO NF as compared CeO_2 NF and also higher than simple NPs-based photocatalysts. A plausible explanation for the role of NFs over the simple NPs-based photocatalytic solution is presented.

Keywords: nanofluids; conductivity; stability; optical band gap and photocatalyst

1. Introduction

The ever-increasing demand for developing strategies towards utilization of waste heat and management of high heat fluxes poses a significant bottleneck and provides the drive to search

for advanced heat transfer fluids. The term "nanofluid (NF)" was introduced by Choi in 1995 at Argonne National Laboratory of USA, referring to the suspension of nanometer-size particles dispersed in a liquid [1]. In the same period, a Japanese group made metal-oxide dispersed NFs [2]. With advances in nanomaterial synthesis and with the proven fact that nanomaterials are known to enhance the thermophysical properties of fluids, a great number of NFs are developed as next-generation heat transfer fluids. and studies on effective thermal conductivities have been extended by many researchers [3–7]. The generally used base fluids for NF formulation are water, ethylene glycol, engine oil, mineral oil, kerosene oil and silicon oil, as applied in a vast range of engineering applications [8]. NFs provide auspicious heat transfer applications in the industrial sectors and essential fields such as electronics, transportation and medical applications, etc. [9]. The NFs based on metal oxide nanoparticles (NPs) have been prepared and investigated by several researchers such as Choi [1], Das et al. [10], Xuan et al. [11], Eastman et al. [12] and Lee et al. [13]. These studies demonstrated that great enhancement of thermal conductivity (5%–60%) could be deduced over the smaller range of volume fractions (0.1%–5%). The metal oxide nanomaterials that are commonly used for NFs are TiO_2, CuO and Al_2O_3 [14,15]. Keeping in mind the expanding applications, there is a need for the fundamental understanding of the physicochemical properties and a comparison of the behavior of new kinds of metal oxide-based NFs in order to expand their potential benefits and applications in diversified areas that include photocatalysis.

The synthesis of nanoscale transition metal oxides (such as ZnO, TiO_2, Fe_2O_3, and CuO) is of significant interest owing to their intriguing physicochemical properties, such as enhanced catalytic activity, high thermal conductivity and availability of economical and scalable synthetic routes [16–29]. CuO is an indirect bandgap semiconductor with a narrow bandgap of 1.2 eV, an optical absorption depth of around 500 nm and a carrier diffusion length of about 200 nm. CuO finds widespread application as heterogeneous catalysts and recently as photocatalysts [30–32]. The enhancement in the thermal conductivity has been investigated for CuO-ethylene glycol NFs [33]. CuO/dimethicone NFs were prepared with CuO nanowires and spherical NPs and thermal conductivity increments were critically evaluated based on the influence of nanomorphology [34]. With respect to CuO NFs, there are limited reports available based on NFs prepared in a range of conditions [10,35–39]. However, to our knowledge, none of these kind of reports on the CuO based NFs describe the photocatalytic property of the NFs.

Cerium oxide (CeO_2) is a typical fluorite-structured compound containing a cubic close-packed array of metal atoms with eight coordinate Ce^{4+} and four coordinates O^{2-}. The high mobility of oxygen vacancies and the Ce^{4+}/Ce^{3+} reversible characteristics make CeO_2 a key ingredient for catalytic applications and reactions. The vacancies in CeO_2 crystal structure also enable binding of the adsorbate molecules more strongly than normal oxide sites and assist in their dissociation [40,41]. Various kinds of nanostructured CeO_2 have been prepared and utilized for catalytic applications. CeO_2 NPs-based photocatalysts were also developed [42]. Oxygen vacancies are effectively utilized for photocatalysis [43], as they can lead to band-bending and enhance electron-hole pair separation. The Ce^{3+} ions that are present on the CeO_2 crystal surface act as the surface sites for catalysis and photocatalysis. Recently, Jiang et al. compared the heterogeneous photoreactivity of CeO_2 NPs towards photocatalytic oxidation of volatile organic compounds and O_2 evolution [44]. The relatively inactive octahedron CeO_2 was transformed into photoactive CeO_2 by growing prism arm [45]. The photocatalytic activities of CeO_2 nanotubes and NPs were compared with commercial TiO_2 (P25) [46]. Synthesis and characterization of a stable, thermo-conductive oil-based CeO_2 NFs have been reported [47]. Ceria–ethylene glycol (EG) NF was prepared with ceria NPs having diameters ranging between 30 and 50 nm [48]. The studies on transport properties of ceria–EG NFs revealed the viscosity reduction and thermal conductivity enhancement over a range of nanoparticle concentration (0–1 vol%) and temperature. Spherical ceria NPs of the sizes in the range of 18–25 nm were used to prepare ceria-propylene glycol NFs [49]. Energy and environmental protection are two important areas that many of the countries and decision-makers are giving major importance and concern. The elimination

of environmental pollution and the transfer of thermal energy with a common NF will be the most ideal area for in-depth studies. In this work, we showed interest on evaluating the photocatalytic efficiencies of NFs based on two oxide materials, namely CuO and CeO_2. The former is a transition metal oxide and the latter is a lanthanide series (inner transition) metal oxide, respectively. Both of the selected metal oxides (CuO and CeO_2) exhibit photocatalytic properties but have different origins for the photoactivities due to their electronic configurations. On perusal of the literature, one can notice that photocatalytic activities of CuO and CeO_2 nanostructured materials have been evaluated through simple dispersion in water. We ensured effective dispersion of CuO and CeO_2 nanoparticles (NPs) through ultrasonic vibrations while formulating NFs. We believe that a comparative evaluation of the photocatalytic activities between the two selected metal oxides in NF form would be an interesting aspect for investigation. To the best of our knowledge, there is no report available on the comparative account of physicochemical properties and photocatalytic applications between CuO and CeO_2.

In view of the above facts, the present work aims on; (i) preparation of water-based CuO and CeO_2 NFs for a range of concentrations of the respective metal oxide NPs, (ii) comparative evaluation of the few of the physicochemical properties that can influence the photocatalytic efficiencies, and iii) comparative evaluation of photocatalytic degradation capabilities of the NFs on a chosen dye. Methylene blue (MB) is used as the representative organic dye for photocatalytic degradation studies. Herein, the photocatalytic activities of CuO and CeO_2NFs were evaluated in terms of the photodegradation of MB. The present work discusses these aspects.

2. Results and Discussion

In this work, our interest is to demonstrate the utility of CuO (surface area = 35 m^2/g) and CeO_2 (surface area = 20 m^2/g) NPs, in the form of nanosuspensions or NFs, as the photocatalyst for a model reaction. The prepared NFs were used as the new photocatalysts against a specific reaction, degradation of a dye (methylene blue (MB)). There could be a large number of quantifiable parameters associated with the complex photocatalytic processes during the photodegradation of the dye. For example, the photocatalytic processes involved in MB photodegradation are expected to involve a number of events such as photon absorption, exciton separation, carrier separation, carrier transport, electrochemistry and mass transport. These events can be influenced by the parameters such as absorbance / reflectance / scattering, viscosity activity coefficient, activation energy, effective mass (density), dielectric constant/dielectric loss, diffusion coefficient, electric field, drift current, current density (charge transfer resistance), charge/electron transfer coefficient (impedance), Zeta potential, pH of the medium, etc. A complete knowledge about the influence of all of these parameters involved in the photocatalytic processes will be useful for good optimization towards achieving the best overall photocatalytic efficiency from the NFs. Of course, this is a time-consuming and tedious task.

Alternatively, the quantitative descriptions of at least a few of the associated physical and chemical properties of the NFs that can influence the events/parameters in the photocatalytic processes and the overall photocatalytic efficiency can be deduced through experimental studies. In this work, we have selected a few of the properties that can be quantitatively measured or calculated, and performed adequate measurements and/or calculations to obtain them. We believe that the obtained values of these properties could be integrated in such a way to circumvent the kinetic/energetic bottlenecks of the specific properties/processes. Through the knowledge of these properties, the experimental conditions for the photocatalytic process can be decided to achieve better efficiency for the photocatalytic process. Keeping these aspects in view, we arranged the results and the consequent discussion into three major headings (with subheadings), including (i) materials characterization, (ii) physicochemical properties of the NFs and, (iii) photocatalytic application.

2.1. Materials Characterization

Typical results of microstructural and morphological characterization are presented and discussed. The X-ray diffraction (XRD) pattern of CuO and CeO_2NPs are shown in Figure 1a,b. The XRD

pattern of CuO consists of few crystalline peaks (2θ = 35.5°; 2θ = 38.7°) that agree well with the assignments of JCPDS, File No. 01-0801916 for the monoclinic CuO (Figure 1a). The XRD pattern of CeO_2 (Figure 1b) exhibits mainly reflections that correspond to (111), (200), (220), (311), (222) and (400) planes. These peaks are characteristic of the cubic ceria phase with fluorite structure (JCPDS card number 34-394). The average crystalline size was calculated using Debye–Scherrer formula,

$$D = \frac{K\lambda}{\beta \cos\theta} \quad (1)$$

where D is the crystallite size in nanometers, λ is the wavelength of the radiation (1.54056 Å for CuKα radiation), K is a constant equal to 0.94, β is the peak width at half-maximum intensity, and θ is the peak position. The average crystallite size of CuO and CeO_2NPs is 77 nm and 33 nm, respectively.

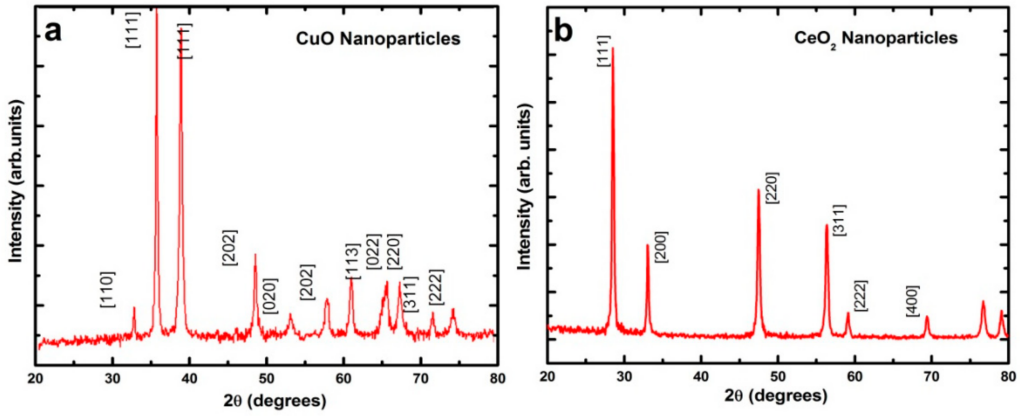

Figure 1. X-ray diffraction pattern of (**a**) CuO NPs and (**b**) CeO_2 NPs.

Scanning electron microscopy (SEM) and transmission electron microscopy (TEM) analysis provide information on the morphology and particle size of the CuO and CeO_2NPs, respectively. The SEM image of CuO NPs (Figure 2a) shows the presence of smaller sized spherical particles with larger agglomerates in different shapes. SEM image of CeO_2 NPs (Figure 2b) reveals the presence of mostly spherical shaped particles with fewer agglomerates. TEM image of CuO NPs (Figure 2c) shows that smaller particles with sizes in the range 50 to 90 nm are spherical and larger particles are agglomerates of smaller particles. TEM image of CeO_2NPs (Figure 2d) shows the narrowly distributed smaller sized spherical particles with a narrow distribution of sizes having the average size of 32 nm, which is in agreement with the XRD results.

The energy dispersive X-ray analysis (Supporting Information–F1) confirms the purity of the metal oxides. The clear presence of the respective metal and oxygen elements only in the copper oxide and cerium oxide samples suggest that there is no contamination.

2.2. *Physicochemical Properties of the NFs*

The viscosity of the NFs depends on various parameters such as nanoparticle volume fraction, base fluid, size of the particle, particle shape, dispersion technique, pH value, temperature, and Brownian motion of NPs. The viscosity can also reveal the particle–particle interactions. Viscosity is expected to play a significant role in the mass transfer process and reaction rate of heterogeneous catalytic reactions. Hence, measurement of viscosity of the NFs becomes important. Relative viscosity (cP) values were determined for CuO and CeO_2 NFs in the concentration range of 0.2%–2.0% at different temperatures 303 K, 308 K, 313 K and 318 K. Supporting Information T1 shows the variation of cP for different concentrations (%) of CuO and CeO_2 NFs with temperatures. Results revealed that cP increases with the metal oxide concentrations (0.2% to 2.0%) and decreases with the increase in temperature (from 303 K to 318 K). The maximum increase in cP was noticed for CeO_2 (9.71%) as

compared to CuO (5.49%) with the respective concentrations (%) of the metal oxides. With regards to temperature effects, a maximum decrease in cP was witnessed for CeO_2 (2.91%) as compared to CuO (1.65%). For both metal oxides, the cP is minimum at lower concentration (0.2%) and steadily increases with higher concentrations (up to 2.0%). The results suggest that frictional forces developed between the layers of NPs in the NFs may be predominant for CeO_2 NPs as compared to CuO NPs. Our results on the viscosity of NFs as a function of temperature at different concentrations of the metal oxides (CeO_2 and CuO) in the concentration range from 0.2% to 2.0% revealed that the viscosity of NFs increases with temperature. This observation was true for the studied concentration range of both metal oxides. An increase in the viscosity can be attributed to higher suspension concentration of the NPs in water, causing higher internal viscous shear stresses [50]. In one of the earlier reports, there was no significant change in the viscosity of NFs over a wider concentration range from 1 to 10 wt.% CuO [51]. The viscosity increase of NFs, as witnessed in this work, with increasing temperature is explained by the fact that the increase in temperature does not weaken the intermolecular forces between the NPs and the base liquid (water) in NFs [52].

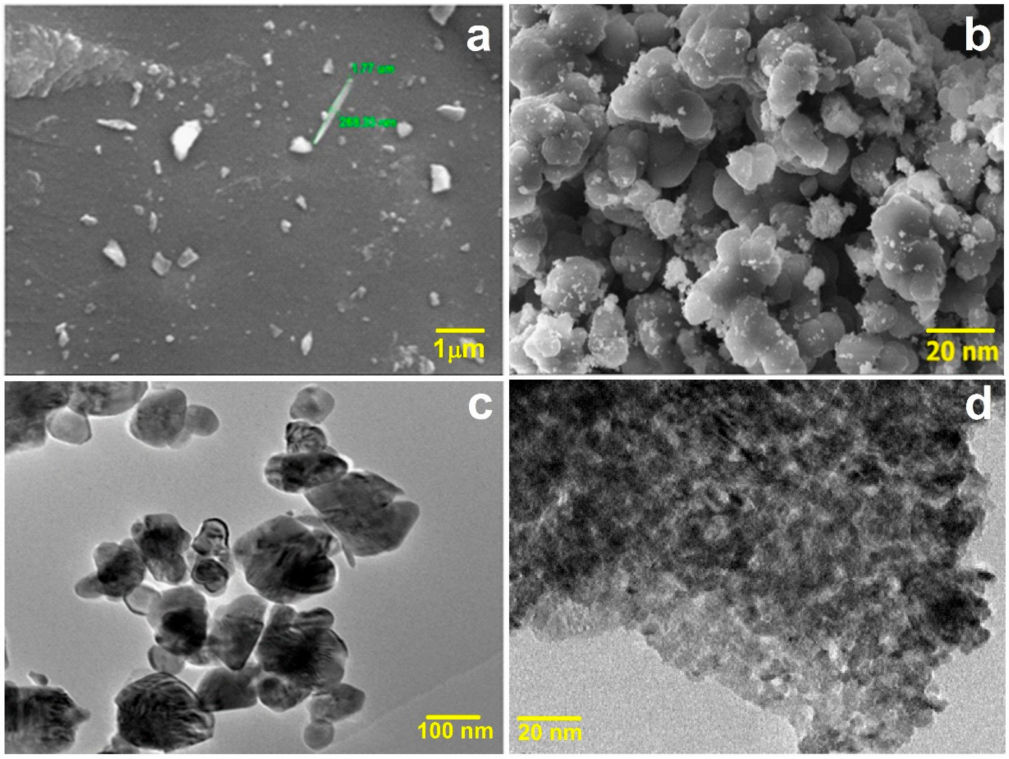

Figure 2. SEM images of (**a**) and (**b**) are CuO and CeO_2, (**c**) and (**d**) are HR-TEM images of CuO and CeO_2, respectively.

The Arrhenius expression was used for representing the activation energy, according to Moore et al. [53],

$$\eta = Ae^{Q/RT} \quad (2)$$

where Q is the apparent activation energy of flow and A is the pre-exponential term with an activation entropy significance. The logarithm of this equation informs a straight-line-type relation.

$$\ln\eta = \ln A + (Q/R)1/T \quad (3)$$

The existence of water in photocatalytic systems influences the activity of the catalytic NPs and activation energy of the photocatalytic processes [54]. Figure 3 shows the variation of the logarithmic

value of viscosity (lnη) against inverse of temperature (1/T) for CuO NFs (Figure 3a) and CeO_2 NFs (Figure 3b). The plots of lnη against 1/T are linear in all of the cases.

The activation energy (Q) is deduced from the slope of these curves (Figure 3a,b). The variation of activation energy Q with the concentration of metal oxides (CeO_2 and CuO) is given in Supplementary Information F2. It has been hypothesized to explain the parameters influence the activation energy in heterogeneous photocatalysis [55]. It has been reported that the apparent activation energy increased at lower temperatures (between 233 and 273 K), and at temperatures higher than 353 K, it changed to negative. In addition, the activation energy values for the photocatalytic reactions were lower than thermal reactions in the intermediate temperatures [56]. From Supplementary Information F2, one can notice that the Q of NFs in the case of CeO_2 NPs showed a sharp increase upon increasing the concentration from 0.2% to 0.4%, and thereafter dropped and varied. Typically, with increase in concentration of CeO_2 NPs from 0.2% to 0.4%, the Q value increased nearly 2.6 times in magnitude. However, in the case of CuO NPs-based NFs, the dependence of Q on concentration was almost independent for the concentration range 0.2% to 0.6%. A gradual increase and decrease in activation energy were noticed between 0.6% and 1.4%. Beyond the concentration of 1.4%, the activation energy remained nearly constant. The results are in corroboration with the probable percolated-like viscosity changes because of the probable collisions between water molecules and metal oxide NPs. Thus, in the present study, it is observed that for CuO and CeO_2 NFs, there is a sudden decrease in the activation energy after 1.0% concentration for CuO and after 0.4% concentration for CeO_2 NFs. In most cases, Q for the viscous flow of fluids increases continuously with increasing particle concentration, except in particular cases of critical combinations. The decrease in Q with the particle concentration for the viscous flow of solutions in poor solvent is attributed to the temperature dependence of the limiting viscosity number [57].

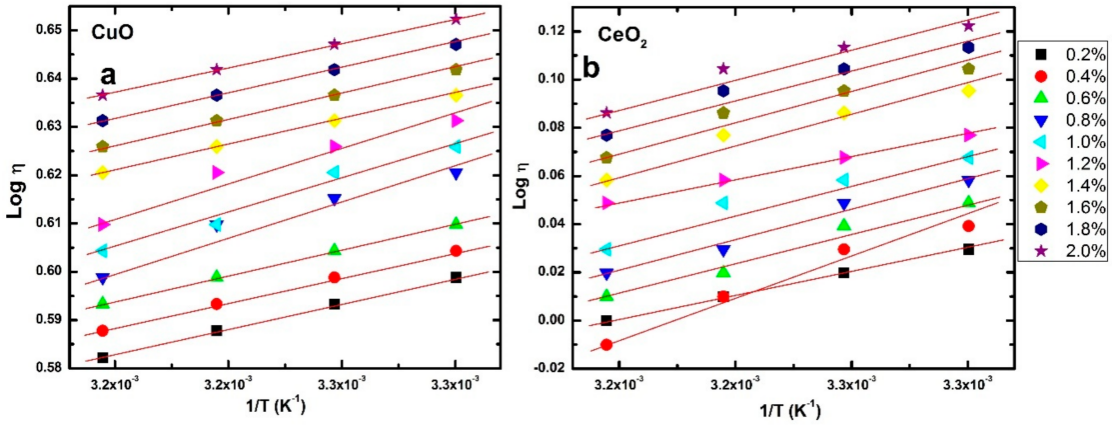

Figure 3. Variation of 1/T against Log η for (**a**) CuO NFs and (**b**) CeO_2.

2.2.1. Density

With the view of characterizing the volumetric behavior of metal oxide (CuO and CeO_2)-based NFs, density measurements were made at concentrations ranging from 0.2% to 2.0% in weight fractions. The density results show a uniform increase with the increase in concentration of CuO and CeO_2 NPs in the NFs at 303 K (Figure 4). While densities of the metal oxides (CuO and CeO_2) are nearly the same in the lower concentration (from 0.2% to 0.6%), an increasing trend in density was seen in both metal oxide-based NFs for a higher concentration range (>0.6%). The density of CuO tends to be lower as compared to CeO_2 in concentrations above 0.6%. This density enhancement for NFs above a concentration of 0.6% may be attributed to either the interfacial effects of the bulk fluid properties produced by the solid nanoparticle surface, or by the interactions that arise among the solid particles [58]. The density is a maximum with a value of 1011.49 kg/m^3 for CuO and 1012.59 kg/m^3 for CeO_2 NFs at higher concentration range (2.0%).

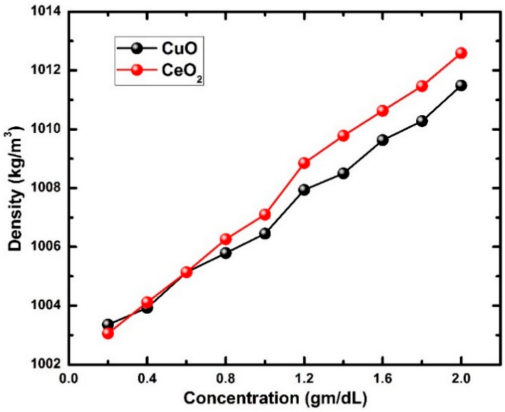

Figure 4. Variation of density with concentration.

2.2.2. Thermal Conductivity

The dispersion of nanosized, thermally conductive particles to liquids has been proven to be a potent strategy to increase the thermal conductivity (k) of the fluid [7]. The first report on k enhancement was copper (Cu) NFs with a lower loading of highly thermal conductive metallic nanoparticles with ethylene glycol as the heat transfer fluid [12]. A 6% enhancement in k was reported with 100 nm sized Cu NPs [59]. A much higher ~24% increase in k was reported with 2 vol% Cu NPs dispersed in gear oil [60]. The bottleneck issue on metallic NP based NF is arcing in high voltage transformer applications. However, a large number of studies on thermal management have been reported on less thermal conductive NPs such metal oxides etc. In particular, the inclusion of micron-sized lesser thermal conductive particles into a heat transfer fluid, such as water, poses a major issue in terms of significant increase in viscosity, abrasion of equipment, aggregation, and settling. The k enhancement in NFs was explained based on few mechanisms that include the concepts of liquid layering around the nanoparticle surface, ballistic phonon transport, Brownian motion induced micro convection and aggregation of nanoparticles [61]. Various factors such as volume fraction (ϕ), nanoparticle size (d), nanoparticle morphology, additives, pH, temperature, nature of base fluid, and nanoparticle morphology, are expected to influence the k of NFs [62–64]. The k values are calculated for CuO and CeO_2 NFs using the mathematical formula,

$$k = 3(N/V)^{2/3}K \quad (4)$$

where k is thermal conductivity, N is Avogadro's number and V is ultrasonic velocity. The thermal conductivity of the two studied NFs increases with the respective NP concentration [34]. Brownian motion of suspended nanoparticles is considered as the major key factor for the noticeable enhancement of thermal conductivity with the nanoparticle addition. Also, the sonication time gives a direct influence on thermal conductivity enhancement. From Supporting Information F3, it is noted that thermal conductivity of CuO NF is greater than CeO_2 NFs. The k enhancements for metal oxide NF typically occur at high particle loading fractions and are dependent on the morphology of the particles. Thus, this information is not typically reported. A nearly 1.18 to 1.54-fold enhancement in thermal conductivity was noticed for the inclusion of 5–16 vol% micron-sized CuO particle loadings [65]. Nearly 9% to 22% enhancements was reported for 6–10 vol% Al_2O_3 loadings [36]. Based on these, it is concluded that the high particle loadings can lead to a significant increase in viscosity and cause an increase in pumping power, negating the advantage of thermal conductivity gain. In the present work, a significantly higher thermal conductivity increase was witnessed for both CuO and CeO_2 NFs with relatively lower particle loadings. The enhancement of k and stability of NF were documented for the monodispersed oleic-acid-capped ceria NPs [47]. It is to be noted that due to the surface functionalization, a long-term stability for the NS was observed. The enhanced thermal conductivity for the surface-functionalized ceria NF was attributed to the small size of particles and the compatibility

of surface-modified nanoparticles with the base fluid. Ceria NPs of a diameter ranging between 30 and 50 nm were dispersed in ethylene glycol over a concentration range (0–1 vol%) and a nearly 10.7% enhancement in k was reported for 1 vol% NF at 30 °C [48]. To the best of our knowledge, this is the first report on the comparative evaluation between water-based CeO_2 and CuO NFs for heat transfer properties.

2.2.3. Electrical Conductivity

In order to understand the electrical properties of the CuO and CeO_2 NFs, various electrical conductivity parameters like impedance, angle, capacitance, resistance, D-factor and reactance were measured using electrochemical impedance analyzer at different frequency range. The electrical conductivity of a NF informs about the ability of charged particles (ions) in the NF to carry the charges (electrons) towards respective electrodes under the applied electric potential. In the case of NFs, the relevant (meta/metal oxide) NPs dispersed in a base fluid (water etc.) creates electrical double layer around the surface of the NPs and NPs along with the EDL move towards oppositely charged electrode surface under the applied potentials. This kind of electric double layer formation depends on the surface charge, size and volume fraction of the particles and ionic concentration in the base fluid. Thus, the electrical conductivity of the NFs is dependent on the electrophoretic mobility of charged particles. Few reports are available on the electrical conductivity of water-based NFs [[66,67]. With relevance to metal oxide-based NFs, electrical conductivity studies were reported on alumina [68]; TiO_2 [66] and a linear increase of electrical conductivity of metal oxide with increasing of particle volume fraction and temperature was observed. Although the electrical properties of NFs are important parameters towards electrical related applications, systematic studies concerning the electrical properties of NFs are limited. In this work, for the first time, we are reporting data on the critical comparison of few of the electrical properties between CuO and CeO_2 in water. The variation of electrical conductivity parameters with frequency is shown in Supporting Information T2. It is observed that the magnitude of impedance decreases with the increase in the applied frequency. Impedance and AC conductivity is found to be inversely related to each other.

The values of angle increase for CuO but CeO_2 show a different trend. The angle values first increase and then decrease at higher frequencies for CeO_2 NFs. The resistance, capacitance and D-factor values of the NFs showed a decreasing trend with increase in frequency. The variation of reactance with frequency of the NFs is also found to decrease with increase in frequency. Using these complex impedance parameters (capacitance, dissipation factor, impedance, resistance, reactance and phase angles), the AC conductivity and dielectric constant of the NPs were calculated.

2.2.4. AC Conductivity Studies

By measuring the conductance (G), thickness and area of pellets of CuO and CeO_2 NPs, the AC conductivity σac(ω) in the frequency range of 100 Hz to 5 MHz is calculated using the equation [69],

$$\sigma ac(\omega) = G(\omega)t/A \quad (5)$$

where t is the thickness of the pellet in cm and A is the area of cross-section in cm^2.The variation of σac (ω) as a function of frequency at room temperature is shown in Figure 5. The value of σac (ω) AC increases with the applied frequency.

We attribute this observation due to the presence of inhomogeneity in the material as the electrical conductivity is associated with the available quantity of free charge carriers and their mobility. This indicates that conduction is due to hopping of charges, and AC conductivity is affected by the mobile charge carriers. The other possibility may be that the polarization of dipoles, i.e., the dipoles rotate between the comparable equilibrium positions. The AC conductivity remains nearly constant for both nanoparticles until 1 MHz, then shows slight variations. The high AC conductivity of CeO_2 NPs is attributed to small polaron hopping at higher frequencies.

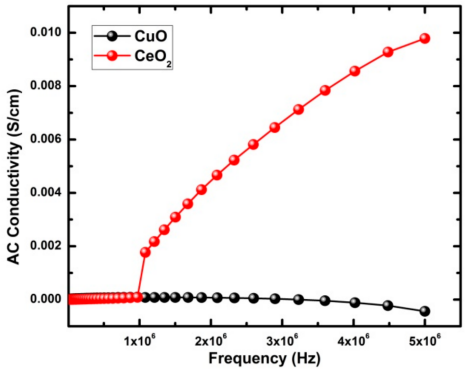

Figure 5. Variation of AC conductivity with frequency.

2.2.5. Dependence of Electrical Conductivity on pH

It has been well demonstrated that understanding the pH influence on NFs helps in the investigations of fundamental nature of many of the properties such as heat transfer, stability, contact angel and electrical conductivity of the NFs. Various factors that include adhesive force and friction present in aqueous NFs depend on their pH values. Also, the physicochemical of ionization in different pHs can influence the electrostatic forces that arise between the charged nanoparticles suspended in the fluids. Hence, the pH of a NF needs to be known to assess the influence on fluid friction, which in turn can be correlated to the viscosity and rheological behavior of NFs. The enhancement mechanism of electrical conductivity of NFs is completely different from thermal the conductivity of NFs. The changes in the pH of SiC–water NF in the range from 5.5 to 10.3 caused a drop in effective viscosity enhancement of the NF [70]. The viscosity and thermal conductivity of Cu–H_2O and Al_2O_3–H_2O NFs were investigated at different pHs. (the viscosity and thermal conductivity of Cu–H_2O and Al_2O_3–H_2O NFs.). Based on results, it was concluded that the NFs were stable and had minimum viscosity enhancements for volume concentration between 0.1 and 0.4%. In the case of copper–water NF, results on the thermal conductivity and Zeta potential dependence for the variations of pH showed that the thermal conductivity reached a maximum at an optimum pH and zeta potential of steadily decreased in the pH between 2 and 9, and thereafter increased [71]. Thermal conductivity and dispersion stability of Al_2O_3–H_2O NFs showed pH dependences between the pH range of 2 and 12 [72]. Studies on zirconium dioxide (ZrO_2) and titanium dioxide (TiO_2) particles-based NFs revealed the pH influence on zeta potential, particle size distribution, viscosity, and thermal conductivity [73]. In another report, the pH influence of Fe_2O_3 (20–60 nm) and CuO (30–50 nm) powder dispersed NFs having three different base fluids: (a) water, (b) ethylene glycol, and (c) water with sodium dodecylbenzene sulfonate surfactant, on zeta potential and thermal conductivity has been detailed [74]. The pH and electrical conductivity of NFs are interrelated and connected through configuration and surface charge of the NPs in the NF suspensions. In the case of NFs, the variations in the degree of ionization with pHs cause changes in electrostatic forces, which in turn alters the electrical properties of the base fluid due to the interactions with the particle surface charges [75]. Similarly, the electrical double layer and electrophoretic mobility of NFs are influenced by pH of the NFs resulting in changes in electrical conductivity [76]. However, a comparative account on the pH influence of electrical conductivity between CuO and CeO_2 NF has not been reported until now. The electrical conductivity and pH values were determined for CuO and CeO_2 NFs over a concentration range from 0.2% to 2.0% at different temperatures and compared (Supporting Information T3. Firstly, the electrical conductivity of the NFs is found to be higher than the base fluid (water). The electrical conductivity and pH values showed variations with concentrations and temperature (Supporting Information T3). It is known that the electrical conductivity of the NFs not only depends on the physical properties of the base fluid and NPs but also greatly influenced by other aspects such as the electrochemical properties, electrical double layers, particle size, and aggregation. It is clear from the table that the electrical

conductivity values of both the NFs increases with increase in concentration and decreases with increase in temperature. A probable explanation for the influence of pH on electrical conductivity is that when the NF concentration is low, 90.2% in this case, the distance between the NPs is relatively larger and the NF is considered to have nearly monodispersed NPs. Consequently, the Zeta potential, the mobility particles and the Brownian motion also increases when the distance between the particles are larger. As an outcome, the electrical conductivity of the NF is increased. The increase in mass and particle size at higher temperatures can cause a decrease in the mobility of the NPs produced by the Brownian motion; as a result, the electrical conductivity enhancement can slow down in higher temperatures [77]. The pH values increase gradually with increase in concentration as shown in Supporting Information T3. It was found that the pH of NFs is greater than that of the base fluid and increases linearly with concentration of NPs.

2.2.6. Stability

The investigation of stability of NFs is vital as it affects the thermophysical and catalytic properties of the NFs. Zeta potential determination gives information on the stability of NFs. As a simple guideline, the colloids with high zeta potential (negative or positive) corresponds to the electrical stabilization, whilst low zeta potentials leads to coagulation or flocculation. In general, a value of 25 mV (positive or negative) can be taken as the arbitrary value that separates low-charged surfaces from highly charged surfaces. The colloids having zeta potential in the range 40 to 60 mV are considered to be good stable. A zeta potential more than 60 mV suggests excellent stability. The obtained values of zeta potential for the present study are shown in Table 1. The CuO NFs have excellent stability at low concentrations (0.2%) and good stability at higher concentrations. CeO NFs have excellent stability at all of the concentration studies in the present work.

Table 1. Variation of Zeta potential with concentration.

Nanofluid	Concentration (%)	Zeta Potential (mv)
CuO	0.2	−200.0
	1.0	−43.4
	2.0	+22.3
CeO_2	0.2	+200.0
	1.0	−200.0
	2.0	−200.0

2.2.7. Refractive Index

The refractive index (RI) of NFs is defined as the ratio of speed of light in vacuum to speed of light in the medium. RI depends on the wavelength, shape, and chemical composition of the NPs. RI correlates to the magnitude of the optical force that an electromagnetic field exerts on NPs [77]. RI studies were performed for the CuO and CeO_2 NFs in the concentration range of 0.2% to 2.0% at 303 K. Supporting Information F4 shows the variation of refractive index against concentration for CuO and CeO_2 NFs at 303 K. In the lower concentration range (0.2%), the RI is the minimum with a value of 1.335 for CuO NFs and 1.334 for and CeO_2 NFs. However, it is noticed that the refractive index is maximum at a higher concentration range (2.0%) with a value of 1.344 for CuO and 1.343 for CeO_2 NFs. In general, it is observed that the refractive index increases with the increase in concentration.

2.2.8. Optical Properties

Optical absorption measurements were carried out for CuO and CeO_2 NP using UV-Vis absorption spectroscopy with the diffuse reflectance spectroscopy technique. Supporting Information F5 shows the variation of the optical reflectance, transmittance and absorbance of CuO and CeO_2 NPs in the

wavelength range of 400–900 nm. Figure 6 presents the absorbance spectra and the bandgap determined by Kubelka–Munk absorption function using the equation [78],

$$(\alpha h\vartheta)^{1/n} = A\left(h\vartheta - E_g\right) \quad (6)$$

where K is the proportionality constant, α is the absorption coefficient and $h\vartheta$ is the photon energy. The exponent n depends on the transition type, whose value for direct transition is $\frac{1}{2}$ and 2 for indirect transition. The shift in the absorption edge with respect to the higher wavelength correlates well with the change in bandgap of the corresponding materials [79,80]. A deep change in the absorbance of CeO_2 is found around 640 nm, which corresponds to narrow bandgap arising from the oxygen vacancy defects [81,82]. In the plot $(\alpha h\vartheta)^2$ versus photon energy $h\vartheta$, the bandgap of CeO_2 and CuO NPs are estimated as 2.1 eV and 1.4 eV, respectively, from the x-intercept as shown in Figure 7.

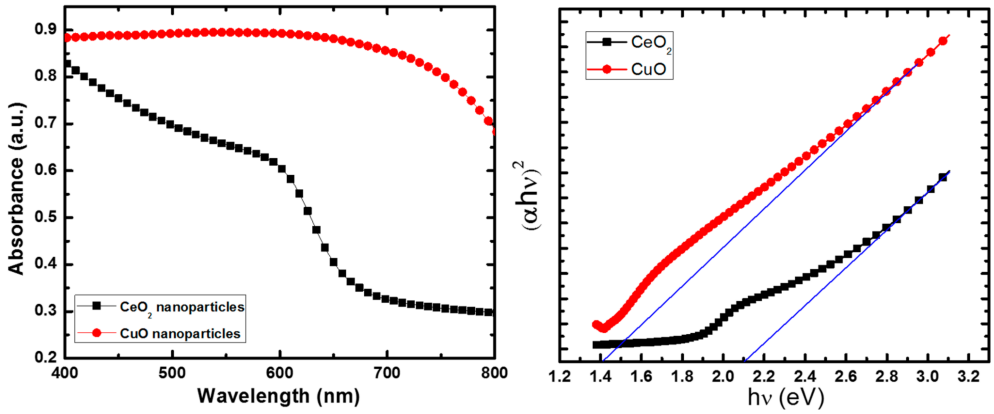

Figure 6. (**a**) Absorbance spectra and (**b**) Kubelka–Munk plot of CuO and CeO_2 NPs.

3. Photocatalytic Studies

Figure 7a,b show the UV-vis absorption spectra recorded during the photoderadation of MB in terms of absorption spectra and as a function of irradiation time under UV light irradiation in the case of CuO and CeO_2 NFs, respectively. The decrease in absorbance at 660 nm informed that the concentration of MB decreased obviously with the increase in reaction time. Several control experiments were carried out to compare the removal efficiencies of MB in the two different systems with identical conditions except in and absence of NFs under UV irradiations. For perusal and reference, snapshots of the MB-containing vessel were taken for the different conditions over various irradiation times are shown in Supporting Information F6. The typical UV-vis absorption spectra recorded for the optimum experimental conditions (CuO NF and CeO_2 NF = 20 mg and MB = 20 mg L^{-1}) are shown in Figure 7a,b. Under UV irradiation, the electron and the hole are generated in the conduction band and in the valence band of CuO and CeO_2, respectively. The positive hole oxidizes the surface oxygen atom/water molecule of CuO and CeO_2 and generates hydroxyl ions and dioxide radicals, respectively. These radicals subsequently cause the degradation of MB [80,81]. Figure 7c shows the percentage of the photo decomposed MB with the reaction time with NFs. The photocatalytic degradation of MB with these NFs is mainly due to the generation of reactive charge carriers of the excited photoactive NPs in the NFs Upon UV light irradiation for 80 min, nearly 100% photodecomposition of MB was witnessed with CuO NFs, whilst CeO_2 needs nearly 120 min for 100% photodecomposition of MB. On perusal of Figure 7c, it is inferred that CuO NF is more efficient photocatalytic system for MB as compared to CeO2. Besides, we noticed that the photodegradation of MB with these NFs follows pseudo-first-order kinetics model, as evidenced by the linear plot of ln(*C*/*C*0) vs. reaction time *t*

(Figure 7d). The pseudo-first-order rate constant for the photocatalytic degradation of MB in CuO and CeO_2 was 0.035 min^{-1} and 0.024 min^{-1}, respectively.

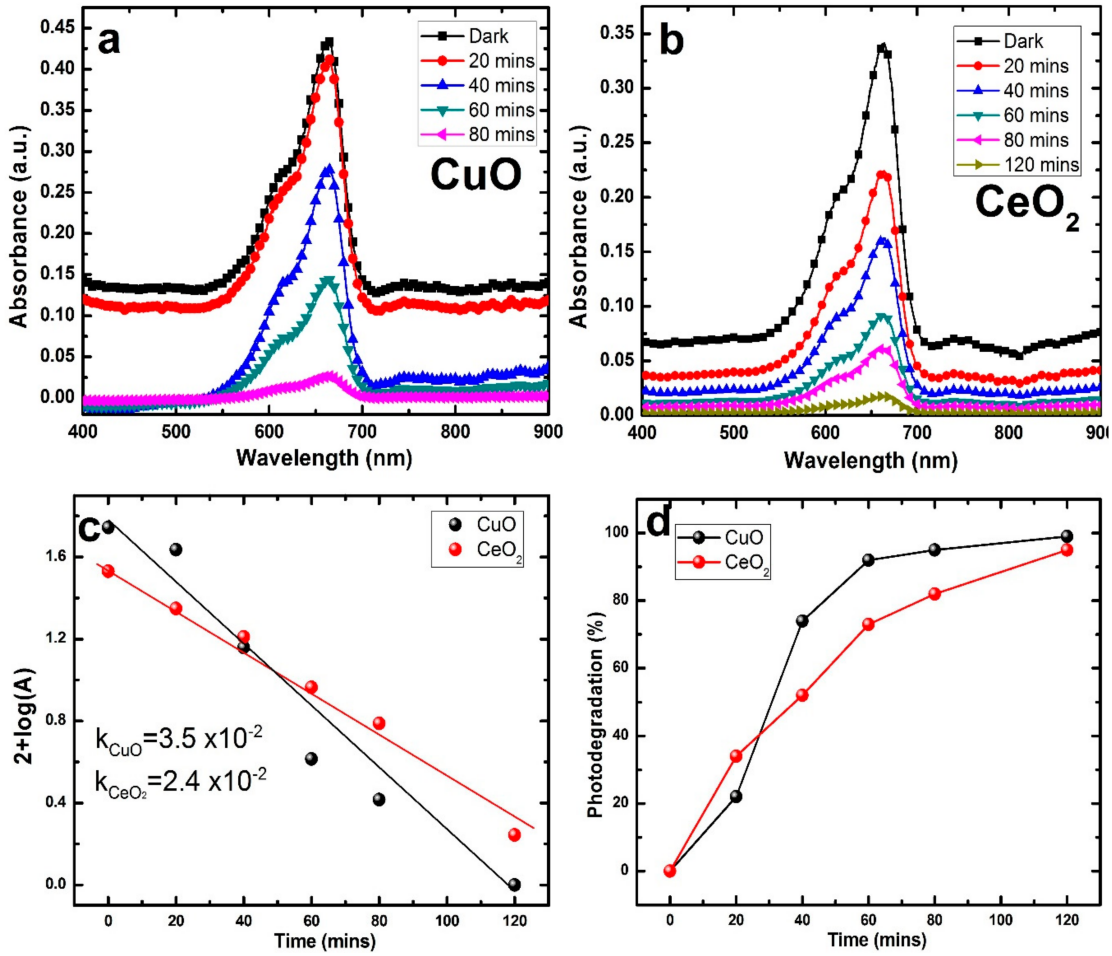

Figure 7. UV-vis absorption spectra of the Methylene Blue solution during the decomposition reaction under UV irradiation in the presence of (**a**) CuO NF and (**b**) CeO_2 NF; (**c**) shows the percentage of the degradation of MB over the reaction time; (**d**) Pseudo-first-order kinetics curves of the degradation of MB under UV irradiation in the presence of CuO NF (**a**) and CeO_2NF (**b**). Experimental conditions: CuO NF and CeO_2 NF = 20 mg and MB =20 mg L^{-1}.

Regarding the present work, the rate of degradation of MB is faster with CuO NF as compared to CeO_2 NF. As a simple explanation, this can be correlated to the higher surface area and porosity of the CuO NPs. However, there can be additional reasons based on the properties of the respective NPs in the NF formulation. Based on the literature, one can notice that CuO NF and CeO_2 NF exhibited higher rate constants for photodegradation of MB than many of the reported rate constants of the conventional nanoparticles-based photocatalysts, such as ZnO (0.022 min^{-1}) [83], TiO_2 (0.025 min^{-1}) [84] and CdS (0.0079 min^{-1}) [85] and also rate constants of the CuO-based nanocatalysts, such as CuO nanowires (0.0046 min^{-1}) [86] and CuO–CuS core–shell nanowires (0.0097 min^{-1}) [86]. Our results gave a clue that the metal oxide nanoparticles—when dispersed in the form of NFs—exhibit enhanced photocatalytic performances. In-depth analysis is underway in our research group to understand the reasons for the enhanced photocatalysis for the NFs, with further studies ongoing regarding other nanoparticles-based NFs.

4. Materials, Characterization and Measurements

4.1. Preparation of Metal Oxide Nanopowder

An aqueous solution of copper acetate (0.02 M) was kept (mL) in a round bottom flask and about 1 mL glacial acetic acid was added (to avoid hydroxylation of Cu^{2+} ions). The solution was stirred vigorously with a magnetic stirrer for 30 min. To the above solution, a solution of NaOH (1M) was dropwise added until the pH reached between 6 and 7. The mixture was stirred for another 10 min at 40 °C. The resultant precipitate was filtered, washed with water and heated to 1000 °C in a muffle furnace. The resultant black powder was crushed and dried to obtain CuO nanopowder. The sample of CeO_2 NPs was purchased (US Nano Laboratories) and used without further purification.

Preparation of NFs

CuO and CeO_2 NPs were dispersed in distilled water to obtain the respective NFs. Ten different concentrations (0.2%–2.0%) in the steps of 0.2% were prepared at room temperature under sonication with a frequency of 24 kHz for about 4 h to ensure effective dispersion of particles.

4.2. Characterization

XRD patterns of the CuO NPs were recorded using the X'Pert PRO pananalytical powder X-ray diffractometer (UK). The diffraction patterns were recorded at room temperature using Cu Kα radiation (k = 1.5406 å) with the Bragg's angle varying from 10° to 80°, with a step size of 0.05°. scanning electron microscopy (SEM) for analyzing high-resolution surface imaging was performed using JEOL JSM-6390 LV (USA) attached with Oxford instruments EDX (UK). High-resolution transmission electron microscopy was measured using JEOL JEM 2100 (Japan) for analyzing the CuO and CeO_2 nanoparticles in the nanofluid. Using the Mittal model of the single-frequency ultrasonic interferometer (2 MHz, F-81 model, India), the ultrasonic velocity measurements were made for all the concentrations of the synthesized NFs at 303 K. The viscosity of the suspensions was carried out for all concentrations at four different temperatures, 303 K, 308 K, 313 K, 318 K using a digital viscometer (Brookfield make). With the specific gravity bottle (5 cc), the density of the NFs was determined. Refractive index studies were made using Abbe's refractometer (Mittal make, India). The electrical measurements were done using 6500B Wayne Kerr precision impedance analyzer (UK) in the frequency range of 100 Hz to 5 MHz at 303 K after applying conducting silver paste to the pellets of pure NPs. The electrical conductivity of the prepared NFs was measured using digital conductivity meter (alpha-06 model, India) at four different temperatures 298 K, 303 K, 308 K and 313 K in the range of 20 mS. The pH values were measured using a digital pH meter (Alpha-01 model, India) at 303 K. The Zeta potential was measured using the Zetasizer Nano ZS90, Malvern Instruments Ltd., UK). The GT Sonic Professional Ultrasonic cleaner (China) was used for sonication purpose, operating at a 40-kHz ultrasonic frequency. UV absorption measurements were made using UV Visible spectrometer (ANALYTIKJENA, Germany).

4.3. Photocatalytic Studies with NFs

The photodegradation of MB was monitored under 8W UV lamp (Excel IMPEX) irradiation at room temperature in open air. The quartz cuvette was used as the reaction vessel. The distance between the light source and the reaction vessel was fixed around 10–12 cm. Typically, the NFs-based photocatalyst prepared with 20 mg of respective NPs photocatalyst was kept in 50 mL of MB aqueous solution (30 mg L^{-1}) in a 50-mL beaker. Prior to irradiation, the photocatalyst included NF was stirred homogeneously for 15 min in dark atmosphere. During the photodegradation reaction, stirring was continuously maintained to keep the stable dispersion of NPs in the NFs. About 2 mL of sample was taken out at regular intervals using a syringe filter and immediately transferred to the reaction vessel.

5. Conclusions

CuO and CeO_2 nanofluids are prepared by a two-step method with the help of a sonicator. The structure and morphology of the CuO and CeO_2 nanoparticles were studied by XRD, SEM, TEM and EDAX techniques. From the measured acoustic parameters, the molecular interaction and thermal conductivity enhancement of the nanofluids are analyzed. The electrical conductivity of the nanofluids were found to increase with an increase in concentration and decrease with an increase in temperature. The stability of the nanofluids are analyzed from Zeta potential measurement. The optical properties of the two nanofluids are studied for possible photocatalytic application. The rate of photodegradation of methylene blue was compared between the CuO and CeO_2 nanofluids. Our results predicted that metal oxide-based nanofluids exhibit enhanced the photocatalytic efficiency in comparison to NPs-based photocatalytic systems. Our results pave the way for further research activities towards exploring the intricate details and mechanisms of photocatalysis in correlation with the properties of the nanofluid systems.

Supplementary Materials: The following are available online at http://www.mdpi.com/2073-4344/10/1/34/s1, Supporting Information F1. EDS image of (a) CuO NPs and (b) CeO_2 NPs, Supporting Information T1; Values of relative viscosity of CuO and CeO_2 NFs, Supporting Information F2; Variation of activation energy with concentration, Supporting Information F3; Variation of thermal conductivity with concentration, Supporting Information T2; Variation of Electrical conductivity parameters of CuO and CeO_2 with frequency, Supporting Information F4; Variation of refractive index with concentration for CuO and CeO_2 NFs; Supporting Information T3. Electrical Conductivity and pH values of CuO and CeO_2 nanofluid with concentration; Supporting Information F5. Variation of reflectance, transmittance and absorbance of CuO and CeO_2 as a function of wavelength.

Author Contributions: R.M., conceptualization, experimentation, data collection, writing; P.R. and V.K., experimentation, writing; V.A.L.R., conceptualization, methodology, visualization; A.-I.G., conceptualization, methodology, data interpretation and writing; G.S., data analysis/interpretation, review and editing; W.-J.K. and V.K., supervision, project administration, funding acquisition and constructive suggestions. All authors have read and agreed to the published version of the manuscript.

Funding: This work was supported by the National Research Foundation of Korea (NRF) grant funded by the Korean government (No. NRF-2018R1A2B2003832).

Conflicts of Interest: The authors declare no conflict of interest.

References

1. Choi, S.U.S.; Eastman, J.A. *Enhancing Thermal Conductivity of Fluids with Nanoparticles*; Argonne National Lab.: Lemont, IL, USA, 1995.
2. Masuda, H.; Ebata, A.; Teramae, K.; Hishinuma, N. Alteration of Thermal Conductivity and Viscosity of Liquid by Dispersing Ultra-Fine Particles. *Netsu Bussei* **1993**, *7*, 227–233. [CrossRef]
3. Hong, T.K.; Yang, H.S.; Choi, C.J. Study of the enhanced thermal conductivity of Fe nanofluids. *J. Appl. Phys.* **2005**, *97*, 064311. [CrossRef]
4. Kim, H.; DeWitt, G.; McKrell, T.; Buongiorno, J.; Hu, L.W. On the quenching of steel and zircaloy spheres in water-based nanofluids with alumina, silica and diamond nanoparticles. *Int. J. Multiph. Flow* **2009**, *35*, 427–438. [CrossRef]
5. Murshed, S.M.S.; Leong, K.C.; Yang, C. Enhanced thermal conductivity of TiO_2—Water based nanofluids. *Int. J. Therm. Sci.* **2005**, *44*, 367–373. [CrossRef]
6. Ali, H.M.; Ali, H.; Liaquat, H.; Bin Maqsood, H.T.; Nadir, M.A. Experimental investigation of convective heat transfer augmentation for car radiator using ZnO–water nanofluids. *Energy* **2015**, *84*, 317–324. [CrossRef]
7. Bhanushali, S.; Jason, N.N.; Ghosh, P.; Ganesh, A.; Simon, G.P.; Cheng, W. Enhanced Thermal Conductivity of Copper Nanofluids: The Effect of Filler Geometry. *ACS Appl. Mater. Interfaces* **2017**, *9*, 18925–18935. [CrossRef] [PubMed]
8. Suganthi, K.S.; Rajan, K.S. Metal oxide nanofluids: Review of formulation, thermo-physical properties, mechanisms, and heat transfer performance. *Renew. Sustain. Energy Rev.* **2017**, *76*, 226–255. [CrossRef]
9. Nabeel Rashin, M.; Hemalatha, J. Acoustic Study on the Interactions of Coconut Oil Based Copper Oxide Nanofluid. *Int. J. Phys. Math. Sci.* **2012**, *6*, 386–390.

10. Das, S.K.; Putra, N.; Thiesen, P.; Roetzel, W. Temperature Dependence of Thermal Conductivity Enhancement for Nanofluids. *J. Heat Transf.* **2003**, *125*, 567–574. [CrossRef]
11. Xuan, Y.; Li, Q.; Hu, W. Aggregation structure and thermal conductivity of nanofluids. *AIChE J.* **2003**, *49*, 1038–1043. [CrossRef]
12. Eastman, J.A.; Choi, S.U.S.; Li, S.; Yu, W.; Thompson, L.J. Anomalously increased effective thermal conductivities of ethylene glycol-based nanofluids containing copper nanoparticles. *Appl. Phys. Lett.* **2001**, *78*, 718–720. [CrossRef]
13. Lee, S.; Choi, S.U.S.; Li, S.; Eastman, J.A. Measuring Thermal Conductivity of Fluids Containing Oxide Nanoparticles. *J. Heat Transf.* **1999**, *121*, 280–289. [CrossRef]
14. Karthikeyan, N.R.; Philip, J.; Raj, B. Effect of clustering on the thermal conductivity of nanofluids. *Mater. Chem. Phys.* **2008**, *109*, 50–55. [CrossRef]
15. Turgut, A.; Tavman, I.; Chirtoc, M.; Schuchmann, H.P.; Sauter, C.; Tavman, S. Thermal Conductivity and Viscosity Measurements of Water-Based TiO_2 Nanofluids. *Int. J. Thermophys.* **2009**, *30*, 1213–1226. [CrossRef]
16. Benzigar, M.R.; Joseph, S.; Saianand, G.; Gopalan, A.I.; Sarkar, S.; Srinivasan, S.; Park, D.H.; Kim, S.; Talapaneni, S.N.; Ramadass, K.; et al. Highly ordered iron oxide-mesoporous fullerene nanocomposites for oxygen reduction reaction and supercapacitor applications. *Microporous Mesoporous Mater.* **2019**, *285*, 21–31. [CrossRef]
17. AnanthaIyengar, G.; Shanmugasundaram, K.; Nallal, M.; Lee, K.P.; Whitcombe, M.J.; Lakshmi, D.; Sai-Anand, G. Functionalized conjugated polymers for sensing and molecular imprinting applications. *Prog. Polym. Sci.* **2019**, *88*, 1–129. [CrossRef]
18. SaiAnand, G.; Sivanesan, A.; Benzigar, M.R.; Singh, G.; Gopalan, A.I.; Baskar, A.V.; Ilbeygi, H.; Ramadass, K.; Kambala, V.; Vinu, A. Recent Progress on the Sensing of Pathogenic Bacteria Using Advanced Nanostructures. *Bull. Chem. Soc. Jpn.* **2019**, *92*, 216–244. [CrossRef]
19. Komathi, S.; Gopalan, A.I.; Kim, S.K.; Anand, G.S.; Lee, K.P. Fabrication of horseradish peroxidase immobilized poly(N-[3-(trimethoxy silyl)propyl]aniline) gold nanorods film modified electrode and electrochemical hydrogen peroxide sensing. *Electrochim. Acta* **2013**, *92*, 71–78. [CrossRef]
20. Gopalan, A.I.; Komathi, S.; Sai Anand, G.; Lee, K.P. Nanodiamond based sponges with entrapped enzyme: A novel ele Fabrication of horseradish peroxidase immobilized poly(N-[3-(trimethoxy silyl)propyl]aniline) gold nanorods film modified electrode and electrochemical hydrogen peroxide sensing ctrochemical probe for hydrogen peroxide. *Biosens. Bioelectron.* **2013**, *46*, 136–141. [CrossRef]
21. Shanmugasundaram, K.; SaiAnand, G.; Gopalan, A.I.; Lee, H.G.; Yeo, H.K.; Kang, S.W.; Lee, K.P. Direct electrochemistry of cytochrome c with three-dimensional nanoarchitectured multicomponent composite electrode and nitrite biosensing. *Sens. Actuators B Chem.* **2016**, *228*, 737–747. [CrossRef]
22. SaiAnand, G.; Gopalan, A.I.; Kang, S.W.; Komathi, S.; Lee, K.P. One Pot Synthesis of New Gold Nanoparticles Dispersed Poly(2-aminophenyl boronic acid) Composites for Fabricating an Affinity Based Electrochemical Detection of Glucose. *Sci. Adv. Mater.* **2014**, *6*, 1356–1364. [CrossRef]
23. Kang, B.H.; Kim, J.S.; Lee, J.S.; Lee, S.W.; Sai-Anand, G.; Jeong, H.M.; Lee, S.H.; Kwon, D.H.; Kang, S.W. Solution Processable CdSe/ZnS Quantum Dots Light-Emitting Diodes Using ZnO Nanocrystal as Electron Transport Layer. *J. Nanosci. Nanotechnol.* **2015**, *15*, 7416–7420. [CrossRef] [PubMed]
24. Lee, H.G.; Gopalan, A.I.; Sai-Anand, G.; Lee, B.C.; Kang, S.W.; Lee, K.P. Facile synthesis of functionalized graphene-palladium nanoparticle incorporated multicomponent TiO_2 composite nanofibers. *Mater. Chem. Phys.* **2015**, *154*, 125–136. [CrossRef]
25. Lee, S.W.; Cha, S.H.; Choi, K.J.; Kang, B.H.; Lee, J.S.; Kim, S.W.; Kim, J.S.; Jeong, H.M.; Gopalan, S.A.; Kwon, D.H.; et al. Low Dark-Current, High Current-Gain of PVK/ZnO Nanoparticles Composite-Based UV Photodetector by PN-Heterojunction Control. *Sensors* **2016**, *16*, 74. [CrossRef] [PubMed]
26. Lee, J.C.; Gopalan, A.I.; SaiAnand, G.; Lee, K.P.; Kim, W.J. Preparation of Visible Light Photocatalytic Graphene Embedded Rutile Titanium(IV) Oxide Composite Nanowires and Enhanced NOx Removal. *Catalysts* **2019**, *9*, 170. [CrossRef]
27. Lee, H.G.; SaiAnand, G.; Komathi, S.; Gopalan, A.I.; Kang, S.W.; Lee, K.P. Efficient visible-light-driven photocatalytic degradation of nitrophenol by using graphene-encapsulated TiO_2 nanowires. *J. Hazard. Mater.* **2015**, *283*, 400–409. [CrossRef] [PubMed]

28. SaiAnand, G.; Gopalan, A.I.; Lee, K.P.; Venkatesan, S.; Qiao, Q.; Kang, B.H.; Lee, S.W.; Lee, J.S.; Kang, S.W. Electrostatic nanoassembly of contact interfacial layer for enhanced photovoltaic performance in polymer solar cells. *Sol. Energy Mater. Sol. Cells* **2016**, *153*, 148–163. [CrossRef]
29. Liu, M.; Liu, R.; Chen, W. Graphene wrapped Cu_2O nanocubes: Non-enzymatic electrochemical sensors for the detection of glucose and hydrogen peroxide with enhanced stability. *Biosens. Bioelectron.* **2013**, *45*, 206–212. [CrossRef]
30. Liu, J.; Jin, J.; Deng, Z.; Huang, S.Z.; Hu, Z.Y.; Wang, L.; Wang, C.; Chen, L.H.; Li, Y.; Van Tendeloo, G.; et al. Tailoring CuO nanostructures for enhanced photocatalytic property. *J. Colloid Interface Sci.* **2012**, *384*, 1–9. [CrossRef]
31. Rao, M.P.; Wu, J.J.; Asiri, A.M.; Anandan, S. Photocatalytic degradation of tartrazine dye using CuO straw-sheaf-like nanostructures. *Water Sci. Technol.* **2017**, *75*, 1421–1430. [CrossRef]
32. Rao, M.P.; Sathishkumar, P.; Mangalaraja, R.V.; Asiri, A.M.; Sivashanmugam, P.; Anandan, S. Simple and low-cost synthesis of CuO nanosheets for visible-light-driven photocatalytic degradation of textile dyes. *J. Environ. Chem. Eng.* **2018**, *6*, 2003–2010. [CrossRef]
33. Liu, M.S.; Lin, M.C.C.; Huang, I.T.; Wang, C.C. Enhancement of Thermal Conductivity with CuO for Nanofluids. *Chem. Eng. Technol.* **2006**, *29*, 72–77. [CrossRef]
34. Zhu, D.; Wang, L.; Yu, W.; Xie, H. Intriguingly high thermal conductivity increment for CuO nanowires contained nanofluids with low viscosity. *Sci. Rep.* **2018**, *8*, 1–12. [CrossRef] [PubMed]
35. Mintsa, H.A.; Roy, G.; Nguyen, C.T.; Doucet, D. New temperature dependent thermal conductivity data for water-based nanofluids. *Int. J. Therm. Sci.* **2009**, *48*, 363–371. [CrossRef]
36. Li, C.H.; Peterson, G.P. Experimental investigation of temperature and volume fraction variations on the effective thermal conductivity of nanoparticle suspensions (nanofluids). *J. Appl. Phys.* **2006**, *99*, 084314. [CrossRef]
37. Namburu, P.K.; Kulkarni, D.P.; Misra, D.; Das, D.K. Viscosity of copper oxide nanoparticles dispersed in ethylene glycol and water mixture. *Exp. Therm. Fluid Sci.* **2007**, *32*, 397–402. [CrossRef]
38. Liu, M.; Lin, M.C.; Wang, C. Enhancements of thermal conductivities with Cu, CuO, and carbon nanotube nanofluids and application of MWNT/water nanofluid on a water chiller system. *Nanoscale Res. Lett.* **2011**, *6*, 297. [CrossRef]
39. Zhu, H.T.; Zhang, C.Y.; Tang, Y.M.; Wang, J.X. Novel Synthesis and Thermal Conductivity of CuO Nanofluid. *J. Phys. Chem. C* **2007**, *111*, 1646–1650. [CrossRef]
40. Henderson, M.A.; Epling, W.S.; Perkins, C.L.; Peden, C.H.F.; Diebold, U. Interaction of Molecular Oxygen with the Vacuum-Annealed TiO_2(110) Surface: Molecular and Dissociative Channels. *J. Phys. Chem. B* **1999**, *103*, 5328–5337. [CrossRef]
41. Campbell, C.T.; Peden, C.H.F. Oxygen Vacancies and Catalysis on Ceria Surfaces. *Science* **2005**, *309*, 713–714. [CrossRef]
42. Primo, A.; Marino, T.; Corma, A.; Molinari, R.; García, H. Efficient Visible-Light Photocatalytic Water Splitting by Minute Amounts of Gold Supported on Nanoparticulate CeO_2 Obtained by a Biopolymer Templating Method. *J. Am. Chem. Soc.* **2011**, *133*, 6930–6933. [CrossRef] [PubMed]
43. Henderson, M.A.; White, J.M.; Uetsuka, H.; Onishi, H. Photochemical Charge Transfer and Trapping at the Interface between an Organic Adlayer and an Oxide Semiconductor. *J. Am. Chem. Soc.* **2003**, *125*, 14974–14975. [CrossRef] [PubMed]
44. Jiang, D.; Wang, W.; Zhang, L.; Zheng, Y.; Wang, Z. Insights into the Surface-Defect Dependence of Photoreactivity over CeO_2 Nanocrystals with Well-Defined Crystal Facets. *ACS Catal.* **2015**, *5*, 4851–4858. [CrossRef]
45. He, Y.; Liang, X.; Chen, B.J.N.R. Globin-like mesoporous CeO_2: A CO-assisted synthesis based on carbonate hydroxide precursors and its applications in low temperature CO oxidation. *Nano Res.* **2015**, *8*, 1269–1278. [CrossRef]
46. Tang, Z.-R.; Zhang, Y.; Xu, Y.-J. A facile and high-yield approach to synthesize one-dimensional CeO_2 nanotubes with well-shaped hollow interior as a photocatalyst for degradation of toxic pollutants. *RSC Adv.* **2011**, *1*, 1772–1777. [CrossRef]
47. Sreeremya, T.S.; Krishnan, A.; Peer Mohamed, A.; Hareesh, U.S.; Ghosh, S. Synthesis and characterization of cerium oxide based nanofluids: An efficient coolant in heat transport applications. *Chem. Eng. J.* **2014**, *255*, 282–289. [CrossRef]

48. Mary, E.E.J.; Suganthi, K.S.; Manikandan, S.; Anusha, N.; Rajan, K.S. Cerium oxide–ethylene glycol nanofluids with improved transport properties: Preparation and elucidation of mechanism. *J. Taiwan Inst. Chem. Eng.* **2015**, *49*, 183–191. [CrossRef]
49. Prabhakaran, M.; Manikandan, S.; Suganthi, K.S.; Leela Vinodhan, V.; Rajan, K.S. Development and assessment of ceria–propylene glycol nanofluid as an alternative to propylene glycol for cooling applications. *Appl. Therm. Eng.* **2016**, *102*, 329–335. [CrossRef]
50. Mahbubul, I.M.; Saidur, R.; Amalina, M.A. Latest developments on the viscosity of nanofluids. *Int. J. Heat Mass Transf.* **2012**, *55*, 874–885. [CrossRef]
51. Manasrah, A.D.; Almanassra, I.W.; Marei, N.N.; Al-Mubaiyedh, U.A.; Laoui, T.; Atieh, M.A. Surface modification of carbon nanotubes with copper oxide nanoparticles for heat transfer enhancement of nanofluids. *RSC Adv.* **2018**, *8*, 1791–1802. [CrossRef]
52. Manasrah, A.D.; Laoui, T.; Zaidi, S.J.; Atieh, M.A. Effect of PEG functionalized carbon nanotubes on the enhancement of thermal and physical properties of nanofluids. *Exp. Therm. Fluid Sci.* **2017**, *84*, 231–241. [CrossRef]
53. Moore, W.R.; Brown, A.M. Viscosity-temperature relationships for dilute solutions of cellulose derivatives, Temperature dependence of solution viscosities of ethyl cellulose. *J. Colloid Sci.* **1959**, *14*, 1–12. [CrossRef]
54. ParrinoOrcid, F.; Conte, P.; De Pasquale, C.; Laudicina, V.A.; Loddo, V.; Palmisano, L. Influence of Adsorbed Water on the Activation Energy of Model Photocatalytic Reactions. *J. Phys. Chem. C* **2017**, *121*, 2258–2267. [CrossRef]
55. Jean-Marie, H. Heterogeneous photocatalysis: Fundamentals and applications to the removal of various types of aqueous pollutants. *Catal. Today* **1999**, *53*, 115–129. [CrossRef]
56. Marye, A.F.; Maria, T.D. Heterogeneous photocatalysis. *Chem. Rev.* **1993**, *93*, 341–357. [CrossRef]
57. Okada, R.; Tanzawa, H. Apparent activation energy for the viscous flow of polymer solutions. *J. Polym. Sci. Part A Gen. Pap.* **1965**, *3*, 4294–4296. [CrossRef]
58. Pastoriza-Gallego, M.J.; Casanova, C.; Páramo, R.; Barbés, B.; Legido, J.L.; Piñeiro, M.M. A study on stability and thermophysical properties (density and viscosity) of Al_2O_3 in water nanofluid. *J. Appl. Phys.* **2009**, *106*, 064301. [CrossRef]
59. Kole, M.; Dey, T.K. Enhanced thermophysical properties of copper nanoparticles dispersed in gear oil. *Appl. Therm. Eng.* **2013**, *56*, 45–53. [CrossRef]
60. Xuan, Y.; Li, Q. Heat transfer enhancement of nanofluids. *Int. J. Heat Fluid Flow* **2000**, *21*, 58–64. [CrossRef]
61. Keblinski, P.; Prasher, R.; Eapen, J. Thermal conductance of nanofluids: Is the controversy over? *J. Nanopart. Res.* **2008**, *10*, 1089–1097. [CrossRef]
62. Evans, W.; Fish, J.; Keblinski, P. Role of Brownian motion hydrodynamics on nanofluid thermal conductivity. *Appl. Phys. Lett.* **2006**, *88*, 093116. [CrossRef]
63. Patel, H.E.; Sundararajan, T.; Das, S.K. An experimental investigation into the thermal conductivity enhancement in oxide and metallic nanofluids. *J. Nanopart. Res.* **2010**, *12*, 1015–1031. [CrossRef]
64. Paul, G.; Philip, J.; Raj, B.; Das, P.K.; Manna, I. Synthesis, characterization, and thermal property measurement of nano-Al95Zn05 dispersed nanofluid prepared by a two-step process. *Int. J. Heat Mass Transf.* **2011**, *54*, 3783–3788. [CrossRef]
65. Wang, X.; Xu, X.; Choi, S.U.S. Thermal Conductivity of Nanoparticle—Fluid Mixture. *J. Thermophys. Heat Transf.* **1999**, *13*, 474–480. [CrossRef]
66. Modesto-Lopez, L.B.; Biswas, P. Role of the effective electrical conductivity of nanosuspensions in the generation of TiO_2 agglomerates with electrospray. *J. Aerosol. Sci.* **2010**, *41*, 790–804. [CrossRef]
67. Cruz, R.C.D.; Reinshagen, J.; Oberacker, R.; Segadães, A.M.; Hoffmann, M.J. Electrical conductivity and stability of concentrated aqueous alumina suspensions. *J. Colloid Interface Sci.* **2005**, *286*, 579–588. [CrossRef]
68. Ganguly, S.; Sikdar, S.; Basu, S. Experimental investigation of the effective electrical conductivity of aluminum oxide nanofluids. *Powder Technol.* **2009**, *196*, 326–330. [CrossRef]
69. Sonal, A.; Sunita, R.; Mriganko, D. Comparative studies of Copper oxide with Aluminium oxide nanoparticles in conventional thermal fluids for its enhanced efficiency as coolant. *Proc. Natl. Acad. Sci. USA* **2013**, *83*, 73–77.
70. Timofeeva, E.V.; Smith, D.S.; Yu, W.; France, D.M.; Singh, D.; Routbort, J.L. Particle size and interfacial effects on thermo-physical and heat transfer characteristics of water-based α-SiC nanofluids. *Nanotechnology* **2010**, *21*, 215703. [CrossRef]

71. Li, X.F.; Zhu, D.S.; Wang, X.J.; Wang, N.; Gao, J.W.; Li, H. Thermal conductivity enhancement dependent pH and chemical surfactant for Cu-H_2O nanofluids. *Thermochim. Acta* **2008**, *469*, 98–103. [CrossRef]
72. Zhu, D.; Li, X.; Wang, N.; Wang, X.; Gao, J.; Li, H. Dispersion behavior and thermal conductivity characteristics of Al_2O_3–H_2O nanofluids. *Curr. Appl. Phys.* **2009**, *9*, 131–139. [CrossRef]
73. Wamkam, C.T.; Opoku, M.K.; Hong, H.; Smith, P. Effects of pH on heat transfer nanofluids containing ZrO_2 and TiO_2 nanoparticles. *J. Appl. Phys.* **2011**, *109*, 024305. [CrossRef]
74. Younes, H.; Christensen, G.; Luan, X.; Hong, H.; Smith, P. Effects of alignment, pH, surfactant, and solvent on heat transfer nanofluids containing Fe_2O_3 and CuO nanoparticles. *J. Appl. Phys.* **2012**, *111*, 064308. [CrossRef]
75. Prasher, R.; Evans, W.; Meakin, P.; Fish, J.; Phelan, P.; Keblinski, P. Effect of aggregation on thermal conduction in colloidal nanofluids. *Appl. Phys. Lett.* **2006**, *89*, 143119. [CrossRef]
76. Rubio-Hernandez, F.J.; Ayucar-Rubio, M.F.; Velazquez-Navarro, J.F.; Galindo-Rosales, F.J. Intrinsic viscosity of SiO_2, Al_2O_3 and TiO_2 aqueous suspensions. *J. Colloid Interface Sci.* **2006**, *298*, 967–972. [CrossRef]
77. Sarojini, K.G.K.; Manoj, S.V.; Singh, P.K.; Pradeep, T.; Das, S.K. Electrical conductivity of ceramic and metallic nanofluids. *Colloids Surf. A Physicochem. Eng. Asp.* **2013**, *417*, 39–46. [CrossRef]
78. Bhattacharjee, A.; Ahmaruzzaman, M. CuO nanostructures: Facile synthesis and applications for enhanced photodegradation of organic compounds and reduction of: P-nitrophenol from aqueous phase. *RSC Adv.* **2016**, *6*, 41348–41363. [CrossRef]
79. Ali, M.M.; Mahdi, H.S.; Parveen, A.; Azam, A. Optical properties of cerium oxide (CeO_2) nanoparticles synthesized by hydroxide mediated method. *AIP Conf. Proc.* **2018**, *1953*, 1–5.
80. Majumder, D.; Chakraborty, I.; Mandal, K.; Roy, S. Facet-Dependent Photodegradation of Methylene Blue Using Pristine CeO_2 Nanostructures. *ACS Omega* **2019**, *4*, 4243–4251. [CrossRef]
81. Channei, D.; Inceesungvorn, B.; Wetchakun, N.; Ukritnukun, S.; Nattestad, A.; Chen, J.; Phanichphant, S. Photocatalytic Degradation of Methyl Orange by CeO_2 and Fe–doped CeO_2 Films under Visible Light Irradiation. *Sci. Rep.* **2014**, *4*, 5757. [CrossRef]
82. Ansari, S.A.; Khan, M.M.; Ansari, M.O.; Kalathil, S.; Lee, J.; Cho, M.H. Band gap engineering of CeO_2 nanostructure using an electrochemically active biofilm for visible light applications. *RSC Adv.* **2014**, *4*, 16782–16791. [CrossRef]
83. Fan, H.; Zhao, X.; Yang, J.; Shan, X.; Yang, L.; Zhang, Y.; Li, X.; Gao, M. ZnO–graphene composite for photocatalytic degradation of methylene blue dye. *Catal. Commun.* **2012**, *29*, 29–34. [CrossRef]
84. Houas, A.; Lachheb, H.; Ksibi, M.; Elaloui, E.; Guillard, C.; Herrmann, J.M. Photocatalytic degradation pathway of methylene blue in water. *Appl. Catal. B Environ.* **2001**, *31*, 145–157. [CrossRef]
85. Jiang, F.; Yan, T.; Chen, H.; Sun, A.; Xu, C.; Wang, X. A g-C_3N_4–CdS composite catalyst with high visible-light-driven catalytic activity and photostability for methylene blue degradation. *Appl. Surf. Sci.* **2014**, *295*, 164–172. [CrossRef]
86. Kao, Y.T.; Yang, S.M.; Lu, K.C. Synthesis and Photocatalytic Properties of CuO-CuS Core-Shell Nanowires. *Materials* **2019**, *12*, 1106. [CrossRef]